energies

Article

An Investigation of Tidal Stream Turbine Wake Development Using Modified BEM–AD Model

Chee M. Pang [1], David M. Kennedy [2] and Fergal O'Rourke [1,*]

[1] Centre of Renewables and Energy (CREDIT), School of Engineering, Dundalk Institute of Technology, A91 K584 Dundalk, Ireland; cheemeng.pang@dkit.ie
[2] Department of Mechanical Engineering, Technological University Dublin, Bolton Street, D07 H6K8 Dublin, Ireland; david.kennedy@tudublin.ie
* Correspondence: fergal.orourke@dkit.ie

Abstract: Tidal stream turbines (TST) are a promising option for electricity generation to meet the ever-increasing demand for energy. The actuator disk (AD) method is often employed to represent a TST, to evaluate the TST operating in a tidal flow. While this method can effectively reduce the computational cost and provide accurate prediction of far-wake flow conditions, it falls short of fully characterising critical hydrodynamics elements. To address this limitation, a hybrid method is implemented by coupling AD with the blade element momentum (BEM) theory, using detailed performance data, such as thrust, to enhance the prediction of the wake effects. This work focuses on the development of a hybrid BEM–AD method using Reynolds-Averaged Navier–Stokes (RANS) turbulence models within computational fluid dynamics (CFD). Two variations and a hybrid modification of an AD model are presented in this paper. The first modified variation is a velocity variation that takes into account velocity profile inflow into the disk's configuration. The second modified variation is a radial variation that integrates the blade element theory into the disk's configuration. The hybrid modified model combines both the velocity profiles influenced and blade element theory in the design and analysis of the actuator disk. Several key investigations on some of the pre-solver parameters are also investigated in this research such as the effect of changing velocity and radial distance on the porosity and loss coefficient of the actuator disk performance. Importantly, this work provides an improved method to evaluate the key wake effects from a TST array which is crucial to determine the power performance of the TST array.

Keywords: tidal energy; CFD; RANS; actuator disk; BEM

Citation: Pang, C.M.; Kennedy, D.M.; O'Rourke, F. An Investigation of Tidal Stream Turbine Wake Development Using Modified BEM–AD Model. *Energies* **2024**, *17*, 1198. https://doi.org/10.3390/en17051198

Academic Editors: Patrick G. Verdin and Andrey A. Kurkin

Received: 23 January 2024
Revised: 20 February 2024
Accepted: 28 February 2024
Published: 2 March 2024

1. Introduction

Marine tidal currents stand out as a promising and renewable energy resource with the advantages of high predictability and consistent availability. This reliability makes them ideal for optimised energy output [1]. To effectively harness this energy resource, the installation of turbines in arrays proves to be the most efficient approach, to ensure maximum power extraction [2]. In recent years, a diverse range of different turbine designs has emerged [3]. Despite the many proposed designs of tidal stream turbines, the configuration that has garnered the most attention, especially in the context of commercial-scale array development, is the three-bladed horizontal axis tidal stream turbine [4]. Numerous tidal stream turbine (TST) arrays have been strategically deployed in highly energetic locations worldwide, in most cases serving as generators to produce electricity for local networks [5].

Employing a TST array stands as an effective strategy for maximising the power extraction from a given tidal energy site, while also contributing to cost reduction by sharing transmission and grid integration systems when compared to individual TST installations [6]. However, the deployability of TSTs in an array is limited by factors such as water depth and bathymetry. Furthermore, the wake generated by TSTs can impact the downstream velocity distribution, introducing turbulence that alters the flow field, and thus affecting energy output. Consequently, investigating the spanwise and streamwise spacing between turbines is important to minimise disturbance induced by TST and maximise energy output [7]. Several experimental and numerical studies have been conducted to improve the understanding of the TST, including aspects like design, environmental impact, and hydrodynamic performance of the TSTs, both individually and in arrays. Numerous studies [8–12] have presented critical experiments suitable for the assessment of turbine performance. The data sets derived from these experiments serve as valuable benchmarks for the validation of numerical models that characterise turbine performance, providing details on local turbine flow details to be determined, which are difficult to obtain using experiments only.

Various approaches exist to numerically model TSTs to predict the response of tidal turbines in response to complex environmental inflow conditions, including their loading, performance, and wake generation. Computational fluid dynamics (CFD) is one such approach used to model TSTs. There are advantages and disadvantages to using CFD, the critical factor lies in striking a balance between detailed simulation of the physics and the computational time and resources required for accuracy [13]. Among the CFD models, the most comprehensive and intricately detailed approach for gaining insights into the wake development of a TST is the fully resolved turbine geometry approach [14,15]. However, this approach requires small time steps to solve the flow field around the turbine, resulting in a high computational demand. For this reason, the fully resolved turbine geometry approach is not always a feasible option when modelling a large array of full-scale turbines to provide considerable predictions of turbine performance and wake flow, especially in environments with a wide range of highly variable flow conditions. Thus, an alternative method is needed to represent the TST in CFD simulations.

Two popular modelling approaches to represent a TST are the actuator disk (AD) and blade element momentum (BEM) theory methods. The coupling of the AD and BEM methods, known as the AD–BEM model for TST array studies, has gained traction in recent years [4,16–20]. The AD is a momentum sources model that describes the force distributions along the rotor blades to determine the overall performance of a turbine with significantly lower computational costs and fast processing time. However, the AD model is typically unable to provide realistic near-field downstream wake results within seven diameters [21]. Consequently, BEM theory has been introduced to the AD model to better describe the momentum source term by imitating the effects of blade twist, chord, lift, and drag characteristics. The BEM–AD model requires a reasonable but inexpensive increase in computational requirements.

There were some limitations to the BEM–AD models presented in this paper. Firstly, the model is non-rotating, therefore eliminating any swirl in the flow, but studies have suggested that the effects of swirl are not significant outside the near-field downstream wake region of the TST [22]. However, in some situations, swirl in the near wake can persist further downstream, potentially influencing the flow boundaries and distorting the wake [23]. Secondly, it is assumed that tip vortices from a rotating turbine blade are ignored due to the actuator disk's inability to replicate these vortices, thereby speeding up the wake velocity recovery rate downstream [24,25]. Thirdly, the BEM–AD model was treated as a steady-state model, keeping it in line with the RANS time-averaged nature. However, a pseudo-transient-state model can be produced to account for the various turbulence parameters [13]. Other approaches have been used to model a TST such as moving reference frame (MRF) and sliding mesh. MRF and sliding mesh approaches can capture the rotational effects of TST such as swirl and blade tip vortices [26] but require very fine grid resolutions around the turbine rotor to capture flow field detail; hence, this is computationally expensive [27]. In recent years, there have been various important studies that focus on the development of vortex flow [28–30]; these have brought MRF and sliding mesh back into the spotlight in array modelling.

Numerous studies have been carried out on TSTs using the RANS-actuator disk model to predict the velocities and turbulence intensities in the wake [21]. Studies conducted by Harrison M.E., et al. [31] and V.T. Nguyen [32] have highlighted the performance of Reynolds-Averaged Navier–Stokes (RANS) actuator disk models in 3-dimensional domains. Similar studies were also carried out in an array study performed by Mycek. P [11], Chawdhary S. [33], and Gaurier et al. [2] to investigate turbine–turbine wake interaction in an array to determine the optimal spacing both spanwise and streamwise. Turbine spacing is one of the most important factors influencing the performance of a tidal array, but its effects on the turbine wake interactions or turbine array efficiency are not yet well understood. Hence, an improved understanding and description of individual turbine wake development could greatly aid in optimising turbine layout or spacing that provides the maximum array efficiency [34].

The work presented in this paper provides details on the investigation carried out on the developed BEM–AD model's ability to predict downstream wake effects for potential future use in an array study. The paper presents an empirical formula approach to better describe the relationship between velocity profile and geometry radial effects on porosity and resistance coefficient of a porous disk, as showcased in the work as two modified variations of the BEM–AD model and a hybrid modified BEM–AD model. All models in this work are validated with experimental measurements by L.E. Myers (2013) [8,22]. The first variation is a modified BEM–AD model to incorporate the influence of inlet velocity profile (i.e., tidal current shear) in the disk configuration, which is known as velocity variation. The second variation, known as the radial variation, modified the BEM–AD model by dividing the actuator disk into radial annular elements; this allows the disk to have a radial variation instead of an overall averaged approach. The radial variation also included corrections such as tip loss correction, etc. to the BEM calculation. Meanwhile, the hybrid modified BEM–AD model is a combination of two of the variations discussed. In the sections below, the theory, methodology, results, and discussions of the modified BEM–AD models are detailed, and finally, some key conclusions are presented.

2. Theory

2.1. Reynolds-Averaged Navier–Stokes (RANS) Equations

The approximated forces exerted on the flow by the turbine are applied as source terms in the RANS equations of momentum conservation given in Equation (1) [35,36] and are solved along with the continuity equation given in Equation (2) [35,36]. The source terms are only applied at elements within the turbine region, and the Einstein notation is used in these equations for brevity given in (2) [35].

$$\frac{\partial(\rho U_i)}{\partial \mathrm{t}} + \frac{\partial(\rho U_i U_j)}{\partial x_j} = -\frac{\partial \mathrm{P}}{\partial x_i} + \frac{\partial}{\partial x_j}\left[(\mu + \mu_t)\left(\frac{\partial U_i}{\partial x_j} + \frac{\partial U_j}{\partial x_i}\right)\right] + S_i \tag{1}$$

$$\frac{\partial U_i}{\partial x_i} = 0 \tag{2}$$

where U_i is the velocity of the water averaged over time, t, x_i is the spatial distance, μ is the dynamic viscosity of water, μ_t is the eddy viscosity, and S_i is an added source term for the momentum equations, using porous disk domain in ANSYS CFX [35], given by:

$$S_i = -K\frac{\rho}{2}u|u| \tag{3}$$

where K is the resistance coefficient which needs to be defined by the user in ANSYS CFX, ρ is the density of the fluid, and u is fluid velocity. The term $u\,|\,u\,|$ is to define the source term as a vector in the direction of the flow.

2.2. Actuator Disk Theory

In the actuator disk theory, a thrust force, F_T, is homogeneously distributed across the disk which represents the tidal current turbine. This concept involves treating the turbine as an actuator disk and making assumptions about the flow using momentum theory, as shown in Figure 1. The presence of the actuator disk causes the stream tube to expand after passing through the disk. The disk extracts energy from the flow and creates a discontinuity across the disk, which results in the velocity decreasing and pressure dropping passing through the disk.

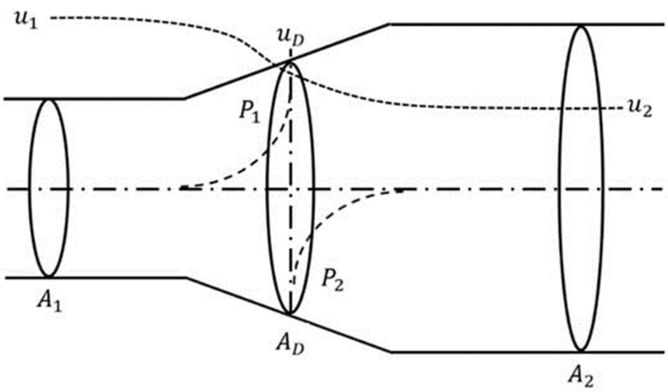

Figure 1. Simple illustration of flow passing through an actuator disk.

However, the disk cannot replicate the swirl caused by the rotating turbine rotor in the near wake between 2D and 5D. Most swirl components of the flow usually dissipate in the near wake and generally play a less significant role in the far wake of the turbine. Despite the limitations, the AD method has demonstrated an ability to model the far-wake condition of the turbine provided that the scale effects are properly parametrised with the suitable production of turbulence. The thrust force acting on the actuator disk results in a discontinuity in pressure, a reduction in kinetic energy of the flow, and a decrease in flow velocity downstream. The thrust force, F_T, is calculated using Equation (4) [37].

$$F_T = \frac{1}{2} C_T \rho A {U_\infty}^2 \tag{4}$$

where C_T is the thrust coefficient, and U_∞ is the upstream flow velocity. According to the Betz limit, the maximum ideal power from the tidal current flow occurs when the axial induction factor, a, is at 0.33, which results in a power coefficient and thrust coefficient of 0.59 and 0.88, respectively. The relationship between the thrust coefficient and the axial induction factor is demonstrated in Equation (5) [22], and the relationship between the power coefficient and the axial induction factor is given in Equation (6) [22].

$$C_T = 4a(1-a) \tag{5}$$

$$C_p = 4a(1-a)^2 \tag{6}$$

According to Taylor [38], a relationship can be formed between the open-area ratio or porosity, θ, and the resistance coefficient, K, as shown in Equation (7). With the consideration of the flow through a porous disk and the use of local velocity, it would be easier to apply a resistance coefficient, K, instead of a thrust coefficient [38]. This relationship has been examined by Harrison [31], which shows this relationship as a reasonable approximation. The resistance coefficient can be determined using the axial induction factor, a, given in (8).

$$\theta^2 = \frac{1}{1+K} \tag{7}$$

$$K = \frac{4a}{1-a} \quad (8)$$

2.3. Blade Element Momentum (BEM) Theory

Blade element momentum (BEM) theory is a combination of momentum theory and blade element theory. It can be used to assess the hydrodynamic performance of a tidal stream turbine blade. BEM theory is utilised by dividing the blade into several elements that are analysed independently [39]. The forces and moments on each local blade element can be obtained by first determining the lift coefficient, C_L, and drag coefficient, C_D. The further integration of the forces over the length of the blade can be used to determine the torque and thrust acting on the turbine rotor [39]. The tangential coefficient, C_{tan}, of each element is calculated using Equation (9), where ϕ is the angle of relative tidal current flow. Using the calculated value of C_{tan} from Equation (9), the local torque developed, dM, is now calculated using Equation (10)

$$C_{tan} = C_L \sin\phi - C_D \cos\phi \quad (9)$$

$$dM = \frac{1}{2} B\rho V_{rel}^2 C_{tan} c dr \quad (10)$$

where B is the number of blades, V_{rel} is the relative tidal current velocity, c is the sectional chord length, and dr is the thickness of the blade element. The overall power developed, P, by the tidal stream turbine blade for the specified tidal current speed is calculated by the sum of all elements for Equation (11), where N is the number of blade elements. The power coefficient, C_P, is calculated by using Equation (12) divided by the power available in the free stream, as shown in Equation (13).

$$dP = \Omega dM \quad (11)$$

$$P = \sum_{i=1}^{N} dP \quad (12)$$

$$C_P = \frac{P}{\frac{1}{2}\rho A {U_\infty}^3} \quad (13)$$

Blade tip loss effects occur as the blade tip is approached. To quantify the blade tip losses, Prandtl's tip loss correction factor, F, can be used as given in Equation (14),

$$F = \frac{2}{\pi}\cos^{-1}\left[\exp-\left(\frac{\frac{B}{2}\left[1-\left(\frac{r_m}{R}\right)\right]}{\frac{r_m}{R}\sin\phi}\right)\right] \quad (14)$$

where R is the radius of the turbine, and r_m is the sectional radius of the turbine. It is necessary to include Glauert's correction model to account for the relationship between the thrust coefficient and axial induction factor when Prandtl's tip loss correction factor is included [40]. Equations (15) and (16) are Glauert's characteristic equations [40] for the thrust coefficient, C_T,

$$C_T = 4\text{aF}(1-\text{a}) \; a > 0.333 \quad (15)$$

$$C_T = \frac{8}{9} + \left(4F - \frac{40}{9}\right)\text{a} + \left(\frac{50}{9} - 4F\right)a^2 \; a < 0.333 \quad (16)$$

Based on Glauert's model [40], the axial induction factor, a, is determined using Equations (17) and (18),

$$a = \frac{1}{1 + \frac{4F\sin^2\phi}{\sigma(C_L\cos\phi + C_D\sin\phi\ )}} \; C_T < 0.96 \quad (17)$$

$$a = \frac{18F - 20 - 3\sqrt{C_T(50 - 36F) + 12F(3F - 4)}}{36F - 50} \; C_T > 0.96 \tag{18}$$

where solidity, σ, can be defined as the ratio of the area of the turbine rotor to the total swept area of the turbine. The local solidity at any specific radial position can be calculated using Equation (19),

$$\sigma = \frac{cB}{2\pi r_m} \tag{19}$$

2.4. BEM–AD Theory

As mentioned, this work coupled both the AD and BEM theory together to explain the porous disk parameters. The momentum loss through the actuator disk is represented in a porous disk as porosity, θ, and the resistance coefficient, K, as seen in Equations (7) and (8). Based on Equation (8), an axial induction factor is needed to describe the resistance coefficient, which can be determined using BEM theory, as shown in Equations (17) and (18). Hence, by combining Equations (17) and (18) into Equation (8) to obtain Equations (20) and (21), which described the resistance coefficient of the porous disk (actuator disk) using BEM theory,

$$K = \frac{\sigma(C_L \cos\phi + C_D \sin\phi\ )}{F \sin^2\phi} \; C_T < 0.96 \tag{20}$$

$$K = \frac{4(18F - 20 - 3k_1)}{18F - 30 + 3k_1} \; C_T > 0.96 \tag{21}$$

where k_1 is a variable described in Equation (22).

$$k_1 = \sqrt{C_T(50 - 36F) + 12F(3F - 4)} \tag{22}$$

3. Methodology

3.1. Introduction

This section details the methodology employed in this work, more specifically the CFD model to predict the downstream wake of a turbine and the model configuration for the variation and hybrid models. Firstly, an overview description of the CFD model is given, followed by a detailed description of the fluid domain and actuator disk domain. Finally, the disk domain is described with a focus placed on the parameters and setup details for each of the variations and hybrid models.

3.2. Computational Fluid Dynamics (CFD) Modelling

Computational Fluid Dynamics (CFD) is a method of analysing a fluid flow field under certain conditions using computational methods. The CFD software used in this work was ANSYS CFX version 2019 R2, which utilises the RANS equation mentioned in Section 2.1. The turbulence model selected in this work was the k-ω Shear Stress Transport (SST) model as it is popular in solving turbulence problems for external flows. The k-ω SST model is a hybrid of k-ω and k-ε turbulence models expressed in k-ω form with shear stress limiting near solid boundaries. However, the actuator disk model has no solid boundaries associated with blades; hence, the model would revert to the k-ε model [41]. Therefore, for these conditions, the k-ω SST model seems to behave similarly to the k-ε model, but the k-ω SST model, according to Johnson, performs better in flows featuring pressure gradients, in terms of accuracy to predict flow properties, this condition is similar to the flow conditions in this work [42]. In this work, the model is assumed to be time-invariant, and the fluid flow field problem was solved in a three-dimensional domain. Before solving a CFD problem using a CFD solver, the following are required: domain construction, mesh development for the domain, and parameter specification for the domain. There were two types of domains constructed in this work, which are the fluid domain and actuator disk domain (porous domain). The two sub-sections below describe the two domain geometries and the parameter setup, while the meshing of the fluid domain is discussed in detail in Section 5.

3.2.1. Fluid Domain

Based on experiments [22,31], the fluid domain in this work has dimensions of 6D (disk diameters) in width, 6D in height, and 20D in length, where the disk is placed in mid-depth of the flow and 5D from inlet, as shown in Figure 2. The domain has a blockage ratio of 6% and a Froude number of 0.18, which were similar to the parameters of expected full-scale tidal sites [22]. In this work, the boundary layer condition is not of specific interest, and the free surface effect is insignificant. Therefore, symmetry conditions are used on the side and top surface boundaries.

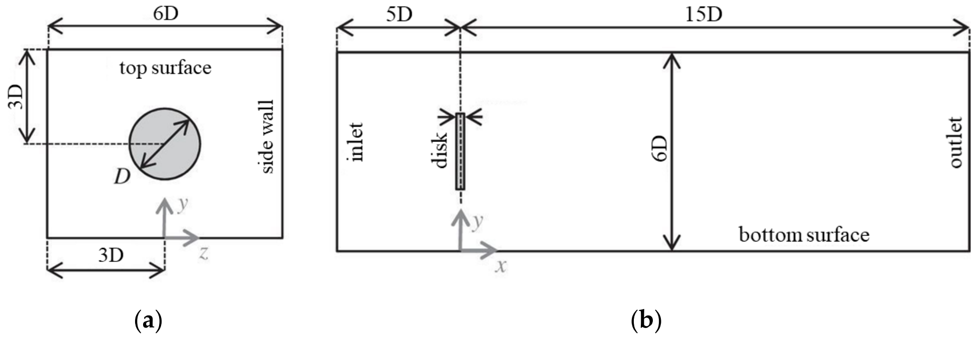

Figure 2. Geometry of the fluid domain: (**a**) Front view; (**b**) Side cross-section view.

The outlet boundary was defined as an opening condition with zero relative pressure and zero turbulence gradients. The bottom surface boundary was described as a smooth wall with a no-slip condition applied. The inlet boundary was described by velocity $U_{inlet}(z)$ profiles and the turbulent kinetic energy $k_{turb}(z)$ profile, as shown in Figure 3. Both of these profiles can be determined using Equations (23)–(25); the numerical profiles match well with the experimental inlet condition [31].

$$U_{Inlet}(z) = 2.5U^{*}ln\left(\frac{zU^{*}}{\nu}\right) + C_V \tag{23}$$

$$k_{turb} = \frac{3}{2}{I_{mean}}^2{U_{mean}}^2 \tag{24}$$

$$\varepsilon = {C_\mu}^{3/4}\frac{{k_{turb}}^{3/2}}{l} \tag{25}$$

where velocity U_{inlet} is the inlet velocity, U^* is the friction velocity, z is the distance from the bottom, C_V is a velocity constant with a value of 0.197 m/s, ν is the kinematic viscosity of water, k_{turb} is the turbulent kinetic energy, U_{mean} is the mean inlet velocity, I_{mean} is the mean turbulence intensity, ε is the turbulent dissipate rate, C_μ is a constant of value 0.09, and l is the turbulence intensity, l = 0.07 H (where H is the characteristic length).

The fluid domain was defined as water with an incompressible fluid setting, and the turbulence model used is the k-ω SST model. The convergence criteria of the simulation were set as RMS residual of value 1×10^{-6}. Table 1 shows a summarised boundary condition of each surface in the fluid domain.

Table 1. Summary of surface boundary conditions.

Surfaces	Boundary Conditions
Top	Symmetry
Sides	Symmetry
Bottom	Smooth Wall with no slip
Outlet	Opening; Entrainment; zero relative pressure and turbulence gradient
Inlet	Velocity condition based on Equations (23)–(25)

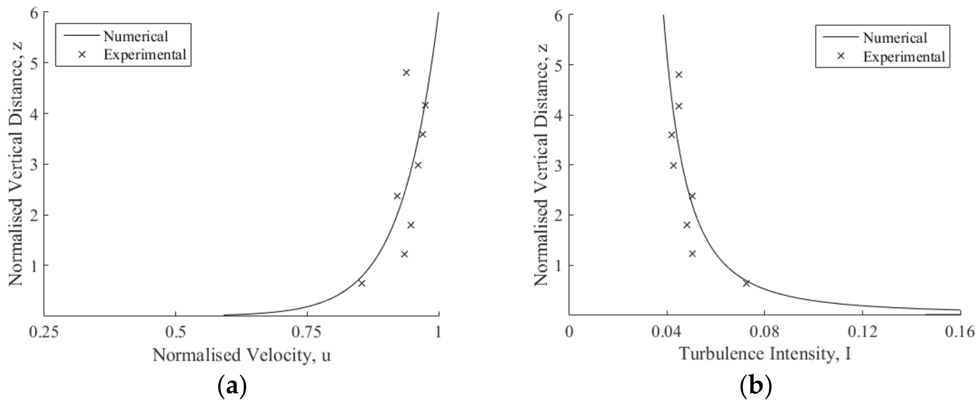

Figure 3. Fluid domain inlet profile: (**a**) Velocity profile; (**b**) Turbulence intensity profile.

3.2.2. Disk Domain and Case Studies Setup

The dimensions of the disk domain have a diameter of 5 m and a thickness of 0.1 m. The disk domain is treated as a porous disk; thus, the porous disk domain needs to be defined in terms of porosity and resistance coefficient, as described in Section 2.2. The BEM–AD model utilises the BEM numerical calculation to calculate the thrust and power coefficient of a tidal stream turbine rotor, which is then used to determine the porosity and resistance coefficient of the porous disk (actuator disk) in the CFD model. In the velocity variation, the disk domain is defined with a non-uniform and varying porosity and loss coefficient due to the velocity profile of the fluid domain. In the radial variation, the disk is divided into 10 annular sections, as shown in Figure 4, and each of the 10 annular sections corresponds to the section of the tidal stream turbine used in this work. The hybrid modified model combines both variations, and each of the annular sections has a non-uniform and variable porosity and resistance coefficient according to the velocity profile. Section 4.4 provides details on the influence of velocity and radial variation on the porosity and resistance coefficient of the disk domain.

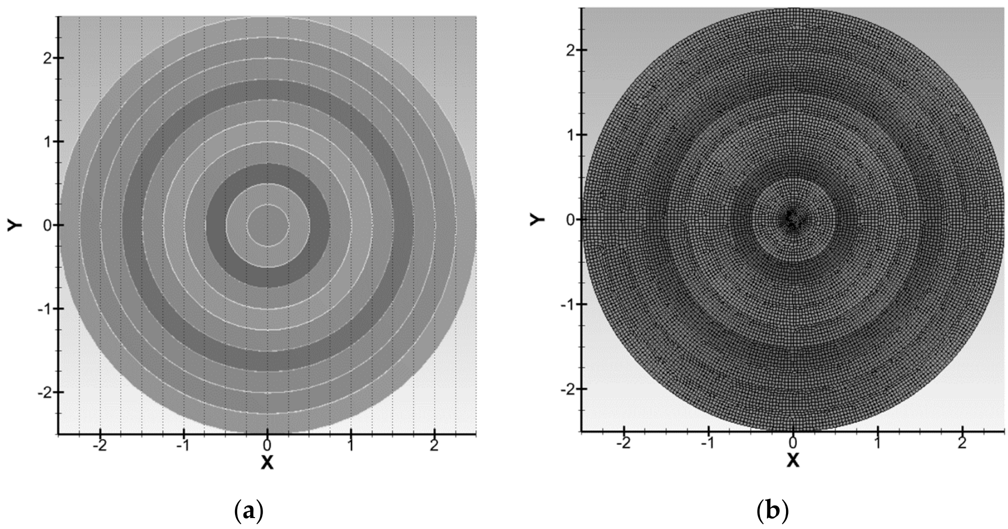

Figure 4. Disk domain for case study view from front: (**a**) Disk dimension; (**b**) Disk mesh.

4. Tidal Stream Turbine Blade Performance

4.1. Introduction

This section presents details of the characteristics of the hydrofoil/spanwise blade section used in this body of work; these characteristics are crucial for numerically modelling the hydrofoil using BEM. The hydrofoil modelling is validated against experimental measurements in terms of power and thrust coefficient at a range of tip speed ratios. The relationship between inlet velocity and TSR can be defined using Equation (26),

$$\mathrm{TSR} = \frac{\omega R}{U_\infty} \quad (26)$$

where ω is the angular velocity of the turbine.

4.2. Blade Characteristic

The tidal stream turbine rotor blade used as a reference in this work is based on the experimental measurements from the work of A.S. Bahaj [8]. The diameter of the rotor is 800 mm, and the blade has a profile shape of a NACA 63-8xx with a chord, thickness, and pitch distribution presented in Table 2. The lift coefficients, C_L, and drag coefficients, C_D, of this hydrofoil can be obtained through a software called XFoil version 6.99.

Table 2. Parameters of the rotor blade [8].

r/R	r (mm)	c/R	Pitch (deg)	t/c (%)
0.2	80	0.1250	20.0	24.0
0.3	120	0.1156	14.5	20.7
0.4	160	0.1063	11.1	18.7
0.5	200	0.0969	8.9	17.6
0.6	240	0.0875	7.4	16.6
0.7	280	0.0781	6.5	15.6
0.8	320	0.0688	5.9	14.6
0.9	360	0.0594	5.4	13.6
1.0	400	0.0500	5.0	12.6

4.3. Power and Thrust Coefficient

A numerical model has been developed to calculate the overall power and thrust coefficient of the TST rotor based on the blade characteristics detailed in the previous sections. The theory used to develop the BEM numerical model is detailed in Section 2. A comparison, for the purpose of model validation, is conducted for the BEM numerical model with measured experimental results [8]. For this comparison, the tidal current fluid speed is set to 1.73 m/s, a background turbulence intensity of 3% is utilised, and a hub pitch angle of 20 degrees is set. The numerical model is constructed using the MATLAB version R2022b software. Figure 5 shows the comparison of the numerical model against measured results in terms of power and thrust coefficient against a range of TSRs. The numerical model shows good agreement with the measured results for both power and thrust coefficient, but there is slight underprediction in thrust coefficient when the tip speed ratio is greater than 7. A further investigation into the numerical model is needed to address this slight underprediction in future work. The tip speed ratio range utilised, in this body of work, ranges between 4 and 7. Thus, the current BEM numerical model is very appropriate for implementation in the BEM–AD model. Thrust Coefficient: C_T.

4.4. Porosity and Resistance Coefficient

The development of the BEM–AD model allows the use of a BEM numerical model in defining the key features required to solve the CFD AD model. Hence, it is crucial to translate the blade performance calculated in the BEM numerical model as inputs into the CFD model to define the AD representation of the TST. The two main crucial elements needed are the porosity and resistance coefficients of the disk domain. As mentioned in Section 3, these two factors can be determined using the thrust coefficient. The porosity and resistance coefficient of the disk domain can be determined using the thrust coefficient, which is an output from the BEM numerical model. As mentioned in the introduction, the two variations and hybrid models carried out in this work have different configurations for the porosity and resistance coefficient of the disk domain.

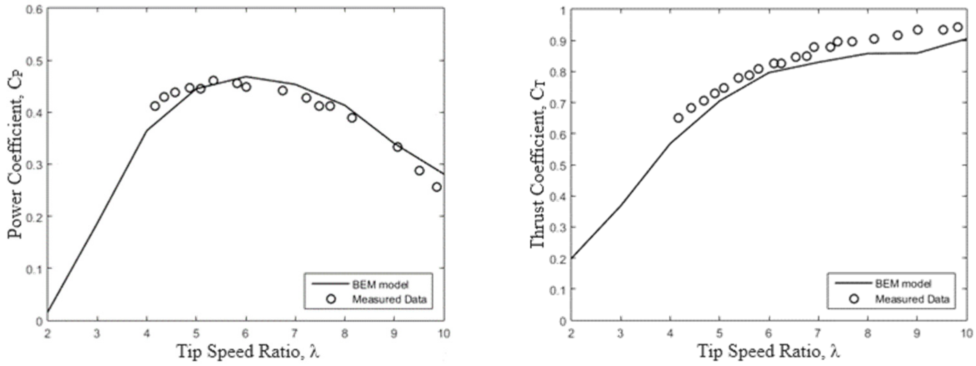

(**a**) (**b**)

Figure 5. Comparison of numerical prediction with experimental measurements [8] for a range of tip speed ratios: (**a**) Power coefficient; (**b**) Thrust coefficient.

The first variation of the developed BEM–AD model is a velocity variation, which takes into account the velocity profile, where the disk experiences a non-uniform incoming velocity, and thus the disk has a varying porosity and resistance coefficient, as shown in Figure 6. The relationship between velocity and porosity is described in Equation (27), and the relationship between velocity and the resistance coefficient is described in Equation (28). It is observed that when velocity increases, the porosity of the disk increases. The resistance coefficient decreases as velocity increases. There is a high correlation between the empirical formula described in Equations (27) and (28) and numerical calculation from BEM calculations of R-square values of 0.9982 and 0.9917, respectively.

$$\theta = -0.076u^3 + 0.369u^2 - 0.307u + 0.608 \tag{27}$$

$$\mathrm{k} = 0.5227u^2 - 2.943u + 4.193 \tag{28}$$

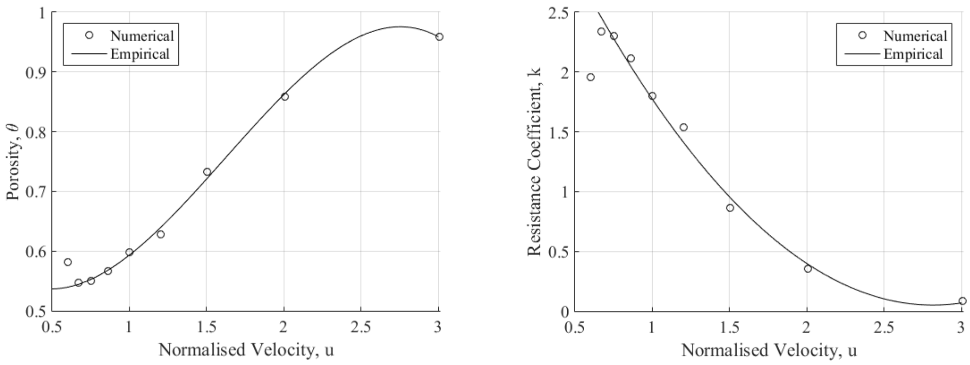

(**a**) (**b**)

Figure 6. The effect of changing normalised velocity on the (**a**) Porosity and (**b**) Resistance coefficient of the velocity variation.

The second variation of the developed BEM–AD model is a radial variation, which incorporates the blade element momentum theory into the design of the disk, and thus the disk has a radial varying porosity and resistance coefficient, as shown in Figure 7. It is observed that as the radius increases, the porosity and resistance coefficient fluctuate around 0.58 and 2, respectively, except for the tip region (at normalised radius, r/R = 1.0). The significant change in porosity and resistance coefficient at the tip region is due to tip loss correction. Hence, one can separate the disk into two different groups of annular sections, which were the body ($0.2 \leq \mathrm{r/R} \leq 0.9$) and the tip (r/R = 1.0). The relationship between radius and porosity of the body region is described in Equation (29), and the relationship between radius and resistance coefficient of the body region is described in

Equation (30). The correlation between the numerical and empirical formulae of the body region has R-square values of 0.936 and 0.932, respectively. The tip region has a numerically calculated porosity and resistance coefficient of 0.52 and 2.75, respectively.

$$\theta = -0.076R^2 + 0.1437R + 0.5472 \tag{29}$$

$$\mathrm{k} = 1.348R^2 - 1.486R - 2.312 \tag{30}$$

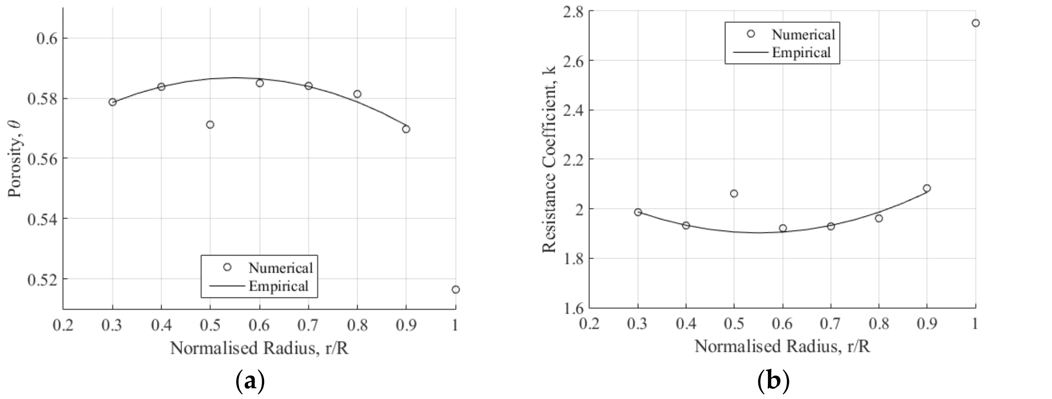

Figure 7. The radially changing (**a**) Porosity and (**b**) Resistance coefficient on the actuator disk with respect to normalised radius of the body region of radial variation.

The hybrid modified BEM–AD model incorporates both variations in describing the porosity and resistance coefficient of the actuator disk. Therefore, there are now two factors affecting the porosity and resistance coefficient, which are the radius of the disk and the velocity profile. The disk domain of the hybrid modified BEM–AD model can also be separated into three sections, where the base (r/R = 0.2) and tip (r/R = 1.0) sections show only velocity variation, as shown in Figures 8 and 9. The relationship between radius and porosity of the base region is described in Equation (31), and the relationship between radius and resistance coefficient of the base region is described in Equation (32). The correlation between the numerical and empirical formulae of the body region has R-square values of 0.9992 and 0.9902, respectively.

$$\theta_{base} = 0.00134\mathrm{u}^3 - 0.034\mathrm{u}^2 + 0.276\mathrm{u} - 0.225 \tag{31}$$

$$\mathrm{k}_{base} = -0.00049\mathrm{u}^3 + 0.012\mathrm{u}^2 + 0.095\mathrm{u} - 1.057 \tag{32}$$

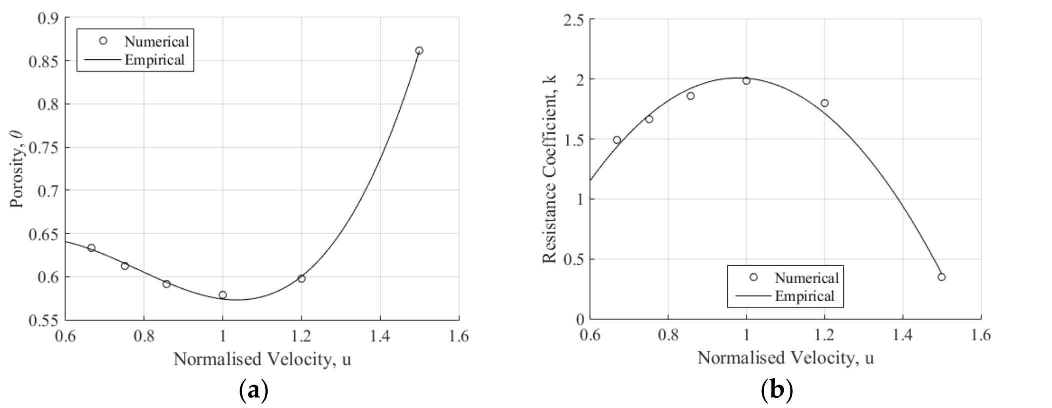

Figure 8. The effect of changing normalised velocity on the (**a**) Porosity and (**b**) Resistance coefficient on the disk's base.

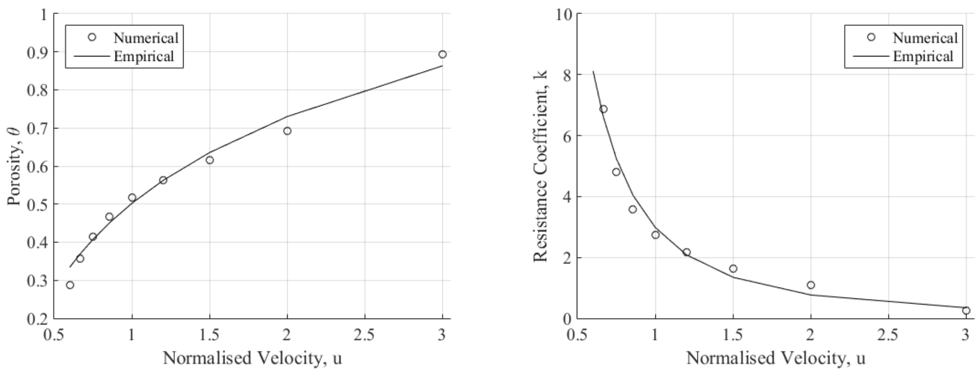

(**a**) (**b**)

Figure 9. The effect of changing normalised velocity on the (**a**) Porosity and (**b**) Resistance coefficient on the disk's tip.

The relationship between radius and porosity of the tip region is described in Equation (33), and the relationship between radius and resistance coefficient of the tip region is described in Equation (34). The correlation between the numerical and empirical formulae of the tip region has R-square values of 0.9830 and 0.9363, respectively.

$$\theta_{tip} = 0.329 \log(\mathrm{u}) + 0.502 \tag{33}$$

$$\mathrm{k}_{tip} = 3.122\mathrm{u}^{-2.05} \tag{34}$$

The body ($0.3 \leq \mathrm{r/R} \leq 0.9$) sections exhibit porosity and resistance coefficient change due to velocity profile and radius, as shown in Figure 10. The relationship between radius and porosity of the tip region is described in Equation (35), and the relationship between radius and resistance coefficient of the tip region is described in Equation (36). The correlation between the numerical and empirical formulae of the tip region has R-square values of 0.9628 and 0.9883, respectively.

$$\begin{aligned}\theta_{body} = 0.5729 \quad & +0.02766\ \mathrm{u}\ + 0.001946\ \mathrm{R}\ + 0.01727\ \mathrm{u}^2 + 0.01921\ \mathrm{uR} \\ & +0.002978\ R^2 + 0.006895\ \mathrm{u}^3 - 0.03471\ \mathrm{u}^2\mathrm{R} \\ & +0.01267\ \mathrm{u}R^2\end{aligned} \tag{35}$$

$$\begin{aligned}\mathrm{k}_{body} = 1.958 \quad & -0.3879\ \mathrm{u}\ - 0.08988\ \mathrm{R}\ - 0.05596\ \mathrm{u}^2 - 0.346\ \mathrm{uR} \\ & +0.04775R^2 + 0.2981\ u^2\mathrm{R}\ - 0.1159\ \mathrm{u}R^2 + 0.0615\ R^3\end{aligned} \tag{36}$$

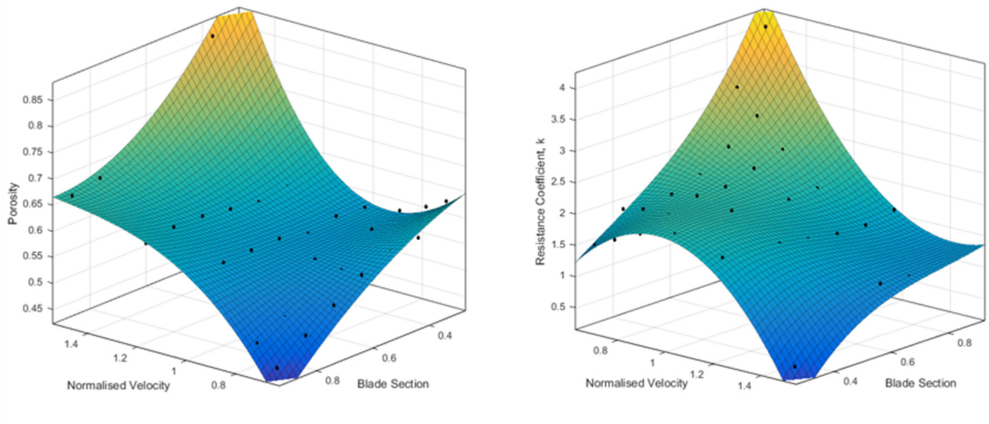

(**a**) (**b**)

Figure 10. The effect of changing normalised velocity and blade section on the (**a**) Porosity and (**b**) Resistance coefficient on the disk's body.

5. CFD Meshing

The model described in Section 3 was executed in ANSYS CFX. Before solving the CFD model, the model required a well-constructed mesh to accurately model the AD representations of the TST. Thus, this section describes the mesh configuration and provides a mesh sensitivity study.

5.1. Mesh Configuration

Using the meshing software available in ANSYS, two domains can be constructed and discretised, which are the fluid domain and the disk domain. The meshing type used in all domains is tetrahedron unstructured mesh and has a smooth transition inflation with a growth rate value of 1.2. The fluid domain constructed is a concentrated mesh fluid domain, as shown in Figure 11. A normal mesh fluid domain in the main mesh domain has a constant element size; whereas in contrast, a concentrated mesh fluid domain has a region with a smaller element size value than the surrounding volume, this region is also known as the region of interest. As the element size decreases in a domain, the number of elements in the domain increases. A higher number of elements tends to give a more accurate result. However, this is dependent on the quality of the mesh. In Figure 11, the sectional side view of a concentrated mesh fluid domain is shown; the region of interest is a semi-circular dome and a cylinder in the regions close to the actuator disk. The semi-circular dome has a radius of 3 disk diameters and is placed before the disk, whereas the cylinder disk has the same radius and is placed directly after the disk with a length extending to the end of the domain. The element size of the region of interest is smaller than the surrounding regions. The reason for this setup is to reduce the computation time of the solver while not sacrificing the accuracy of the results in the region of interest.

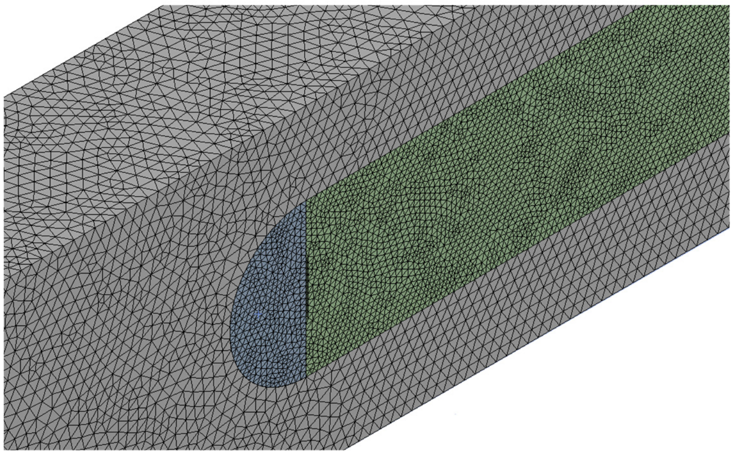

Figure 11. Isometric sectional view of the concentrated mesh fluid domain.

A comparison study between the normal mesh fluid domain and the concentrated mesh fluid domain is carried out. The configuration of the element size in the region of interest in the concentrated mesh fluid domain is the same as the element size in the normal mesh fluid domain, but the surrounding regions have a larger element size. In Figure 12, a comparison is given between the normal mesh and concentrated mesh fluid domain at 5 disk diameters downstream from the disk in terms of velocity and turbulence intensity. The comparison results revealed that there is little difference in terms of downstream velocity and turbulence intensity, particularly in the region of interest. The time required for the normal mesh fluid domain to solve is 2 h 57 min, and the time required for the concentrated mesh fluid domain to solve is 1 h 58 min; these studies were conducted on a Dell desktop PC with 16GB RAM and Intel® Core™ i7-8700 3.20 GHz processor sourced from Dell Technologies, Cork, Ireland, and the solver was run parallel across four processors to further reduce the computational time. A slight overprediction was observed in the velocity prediction outside the region of interest in the concentrated mesh between the normalised vertical distance at 1.5 to 3.0 and −1.5 to −3.0. This can be further improved by decreasing the element size in the area surrounding the region of interest.

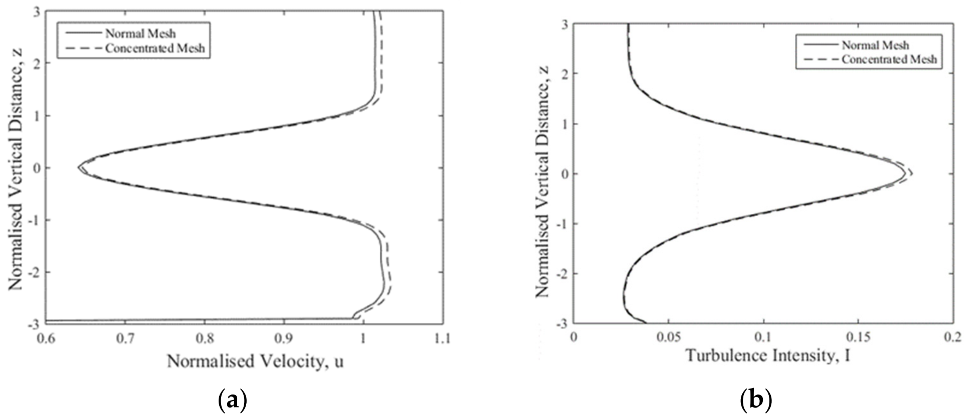

Figure 12. Vertical water column comparison between the normal mesh and the concentrated mesh fluid domain in terms of downstream (**a**) Normalised velocity and (**b**) Turbulence intensity at 5-disk diameters downstream from the actuator disk.

5.2. Mesh Sensitivity Study

An independent mesh study is important in creating an efficient computational simulation while maintaining appropriate accuracy to capture areas of more complex fluid flow behaviour. Five meshes, each with a different number of elements, were investigated and compared for suitability for velocity at six different centreline locations downstream of the actuator disk. These five meshes were produced by reducing the element size in the region of interest, as shown in Table 3, which shows the total number of elements for each mesh setup. These studies were conducted on a Dell PC with 16 GB RAM and Intel® Core™ i7-8700 3.20 GHz processor, and the solver was run parallel across four processors to further reduce the computational time. The mesh independence study was conducted with maximum residuals of 1×10^{-5} and was allowed to run until the solution converged.

Table 3. Total number of elements of 5 different mesh setups.

Mesh	1	2	3	4	5
Element size (m)	0.75	0.50	0.40	0.30	0.15
No. of elements	2.16×10^5	5.18×10^5	9.96×10^5	1.76×10^6	1.13×10^7

The six different point locations, P1 to P6, were taken from the centreline location, with P1 being 2-disk diameters upstream and P2 to P6 located at downstream disk diameters distances of 3, 5, 8, 10, and 15, respectively. Table 4 presents summarised details on the mesh convergence study for each mesh setup and the computational time requirements. A percentage difference between each mesh setup at point locations P2 and P3 is included also. As mentioned earlier, the velocity at P3 converges for Mesh 3 where the percentage difference with Mesh 4 is 0.9% (less than 1%), and the velocity at P2 converges for Mesh 4 where the percentage difference with Mesh 5 is 0.3% (less than 1%). This can be further observed in Figure 13, which shows the velocity at P6 for the range of mesh setups. It is observed that the velocities converge around Mesh 3 for all points with the exception of point 2, which converges for Mesh 4. Point 2 lies within the near-wake region (less than 5 disk diameters from the disk). This being the case, if the study is only interested in results in the far-wake region (more than 5 disk diameters from the disk), then Mesh 3 is suitable. However, the focus of this work is on the near and far-wake regions. Hence, Mesh 4 was selected with a number of elements of 1.76×10^6 and a convergence time of approximately 3 h 44 min.

Table 4. Summary of mesh study for different mesh setups detailing number of elements, normalised velocity at point locations P2 and P3, and convergence time.

Mesh	No. of Elements	Normalised Velocity at Point Location		Normalised Velocity Difference (%)		Convergence Time (hrs: min: sec)
		P2	P3	ΔP2	ΔP3	
1	2.16×10^5	0.835	0.886	-	-	00:58:35
2	5.18×10^5	0.763	0.828	8.6	6.5	01:17:08
3	9.96×10^5	0.732	0.808	4.0	2.4	01:57:08
4	1.76×10^6	0.716	0.801	2.3	0.9	03:44:56
5	1.13×10^7	0.714	0.802	0.3	0.1	08:14:21

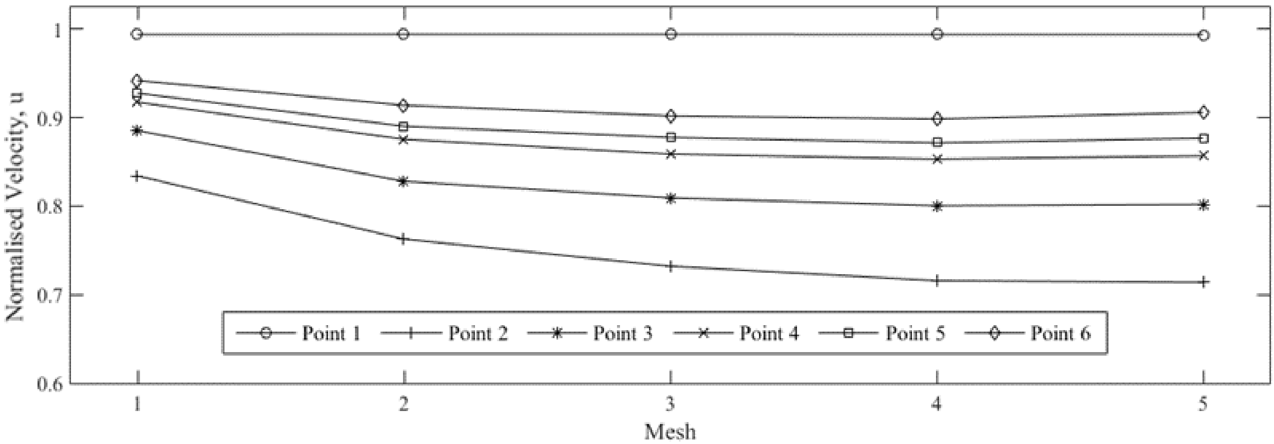

Figure 13. Velocity at six different point locations plotted against different mesh setups, with an increasing number of elements.

6. Results

In this section, the results obtained from the BEM–AD model are presented and discussed. This section contains four sub-sections detailing the capability and suitability of the two variations and hybrid models to predict downstream wake effects in the fluid flow field. The first sub-section presents the velocity variation BEM–AD model, which takes into account the velocity profile of the water column, and the results are compared to experimental measurements [22]. The second sub-section presents the radial variation BEM–AD model, which incorporates the blade element momentum theory method into the disk, and the results are compared to experimental measurements. The third sub-section is the hybrid modified BEM–AD model, which combines both radial and velocity variations to further improve the accuracy of the results. Lastly, the final sub-section provides an overall discussion.

6.1. Modified BEM–AD Model: Velocity Variation

In this sub-section, the developed velocity variation BEM–AD model was validated against experimental measurements. The disk's porosity and resistance coefficient take into account the velocity profile of the water column. Details of this configuration are mentioned in Sections 3.2 and 4.4. Figure 14 shows the centreline downstream velocity and turbulence intensity of the velocity variation BEM–AD model against experimental measurements. The developed model matches well with the experimental measurements, especially after a distance greater than 8D. The model tends to overpredict both velocity and turbulence intensity at downstream distances of less than 7D.

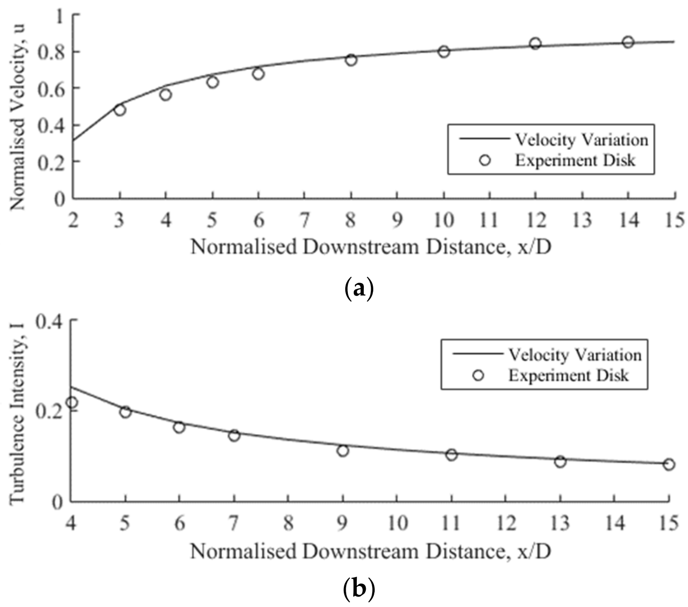

Figure 14. Comparison of downstream centreline (**a**) Velocity and (**b**) Turbulence intensity (bottom) of the velocity variation BEM–AD model against experimental measurements.

Figure 15 shows the downstream velocity and turbulence intensity profile at downstream distances of 5D, 8D, and 10D. The velocity profile at 10D matches closely with the experimental measurements, but for velocity, profile overpredictions occur at 5D and 8D. Whereas, the turbulence intensity is underpredicted at 5D, 8D, and 10D and underpredicted at the centreline region at 5D. The results show that the velocity variation model can predict downstream velocity well at distances greater than 8D. However, it is observed that for vertical depth above the centreline, the model is less accurate compared to below the centreline. The vertical depth below the centreline has a more severe change in vertical velocity profile compared to the vertical depth above the centreline, see Section 3.2.1 for details. This results in the disk having a larger variation in porosity and resistance coefficient below the disk centreline compared to above, which causes the model to describe the downstream wake below the centreline better than above the centreline.

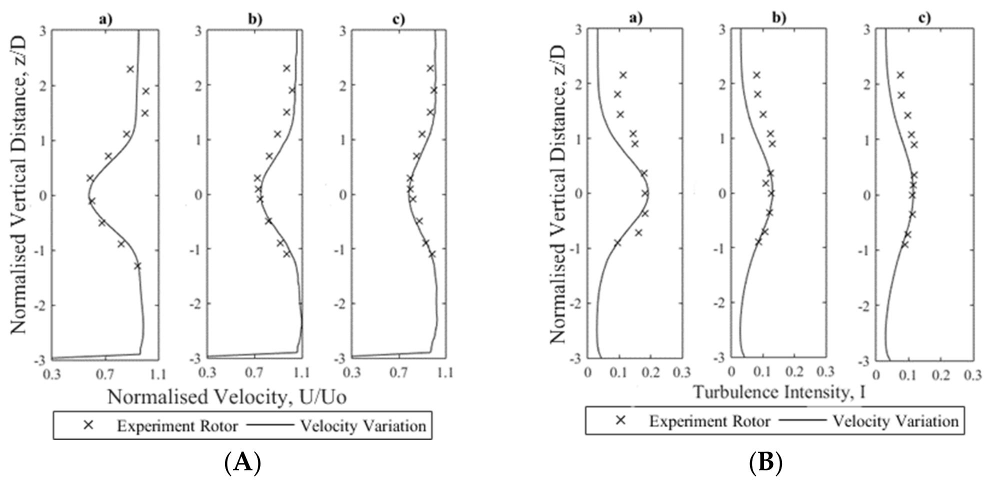

Figure 15. Comparison of (**A**) Vertical velocity and (**B**) Vertical turbulence intensity (right) of the velocity variation BEM–AD model with experimental measurements at downstream distances of (**a**) 5D, (**b**) 8D, and (**c**) 10D.

6.2. Modified BEM–AD Model: Radial Variation

In this sub-section, the developed radial variation BEM–AD model was validated against experimental measurements. The blade element momentum theory method is incorporated into defining the disk's porosity and resistance coefficient. Details of this configuration are described in Sections 3.2 and 4.4. Figure 16 shows the centreline downstream velocity and turbulence intensity of the radial variation BEM–AD model with experimental measurements. The developed model matches well with the experimental measurements, and it seems to be performing better at predicting the centreline downstream wake than the velocity variation BEM–AD model, especially at a downstream distance of less than 8D.

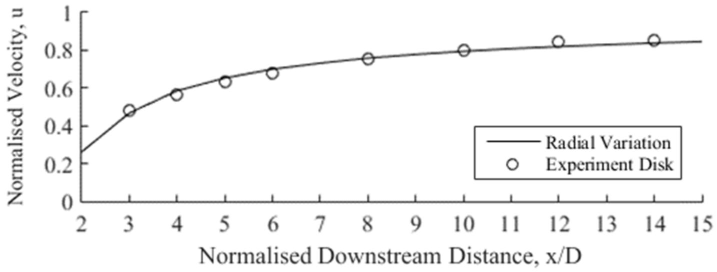

(**a**)

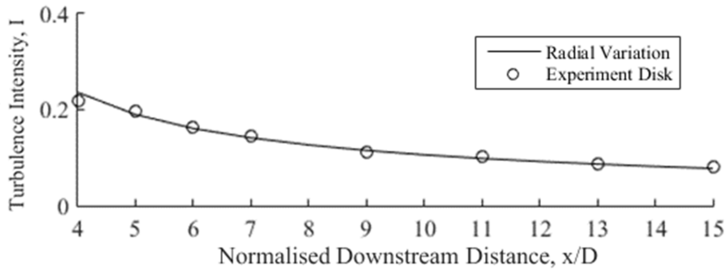

(**b**)

Figure 16. Comparison of downstream centreline (**a**) Velocity and (**b**) Turbulence intensity (bottom) of the radial variation BEM–AD model against experimental measurements.

Figure 17 shows the downstream velocity and turbulence intensity profile at downstream distances of 5D, 8D, and 10D for the radial variation BEM–AD model. The velocity profile at 10D matches well with the experimental measurements in both downstream velocity and turbulence intensity. It is noticed that downstream velocity matches closely with the experimental measurements around the depth region of 1 to −1, while the model outside this region tended to underpredict the results, and the downstream turbulence intensity was shown to be overpredicting around the depth region of 1 to −1. The high accuracy in predicting the downstream velocity at the depth region of 1 to −1 is contributed by the radial variation approach describing the porosity and resistance coefficient of the disk, while it is speculated that outside the depth region of 1 to −1, the wake prediction being less accurate might be due to the velocity profile not being taken into account while describing the disk properties.

6.3. Modified BEM–AD Model: Hybrid Model

In this sub-section, the developed velocity variation and radial variation BEM–AD models were combined to form a hybrid modified BEM–AD model in which both the blade element momentum theory radial approach and the velocity profile in describing the disk properties are taken into account; details of this configuration are described in Sections 3.2 and 4.4. Figure 18 shows the centreline downstream velocity and turbulence intensity of the hybrid modified BEM–AD model against experimental measurements. The developed model matches closely with the experimental measurements; it is shown to be performing better than both the velocity and radial variations. The combination of both variations greatly improves the ability of the hybrid model to predict downstream wake; this can be further observed in the vertical profile of downstream distance 5D, 8D, and 10D in Figure 19.

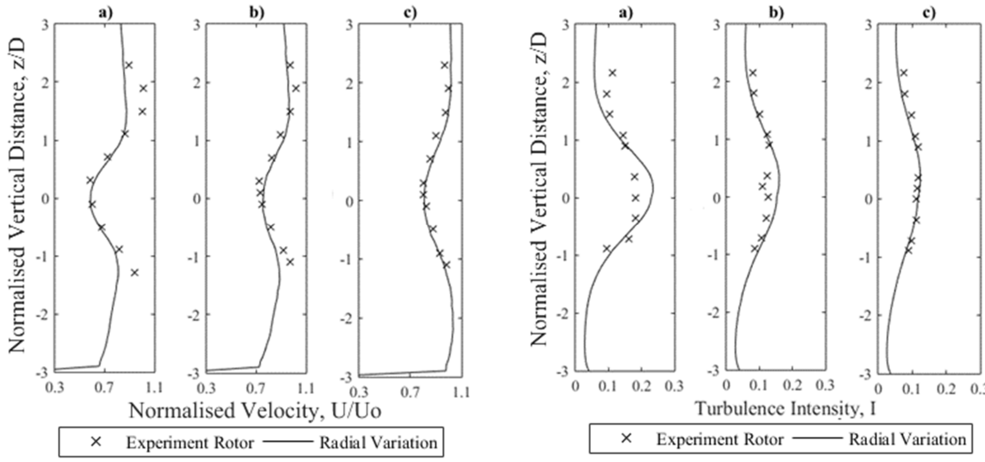

(**A**) (**B**)

Figure 17. Comparison of (**A**) Vertical velocity and (**B**) Vertical turbulence intensity (right) of the radial variation BEM–AD model with experimental measurements at downstream distances of (**a**) 5D, (**b**) 8D, and (**c**) 10D.

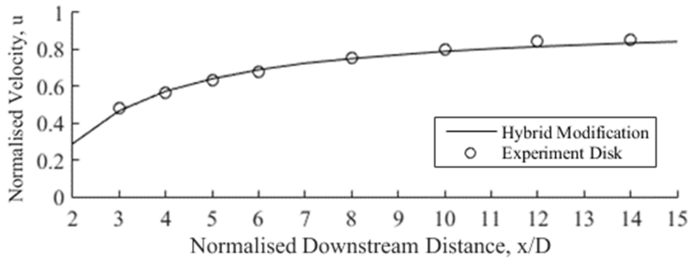

(**a**)

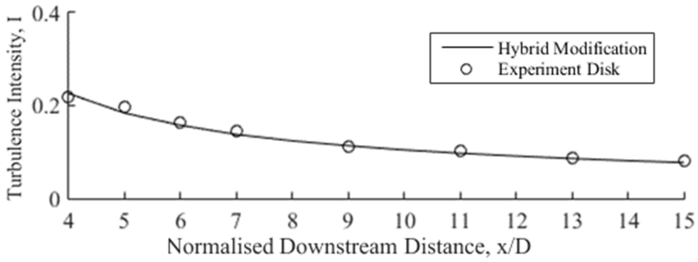

(**b**)

Figure 18. Comparison of downstream centreline (**a**) Velocity and (**b**) Turbulence intensity (bottom) of the modified hybrid BEM–AD model against experimental measurements.

Figure 19 shows the downstream velocity and turbulence intensity profile at a downstream distance of 5D, 8D, and 10D for the hybrid modified BEM–AD model. The velocity profile at 10D matches well with the experimental measurements in both downstream velocity and turbulence intensity. It is observed that the overall wake results greatly improved, especially for all results below the vertical depth of 1. However, the results above the vertical depth of 1 show underprediction in both downstream velocity and turbulence intensity. The reason for this might be due to the developed model not taking into account fluid surface conditions and the surface being treated as a symmetry boundary face. A relationship was observed between velocity and turbulence intensity, i.e., a higher downstream turbulence intensity will result in a higher downstream velocity. This shows that a high turbulence intensity promotes wake velocity recovery.

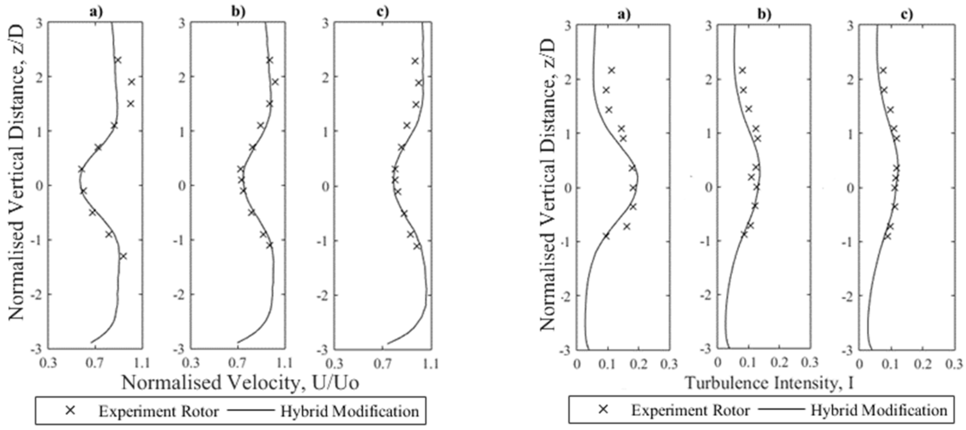

(**A**) (**B**)

Figure 19. Comparison of (**A**) Vertical velocity and (**B**) Vertical turbulence intensity (right) of the modified hybrid BEM–AD model with experimental measurements at downstream distances of (**a**) 5D, (**b**) 8D, and (**c**) 10D.

6.4. Overall Discussion

Overall, the modified hybrid BEM–AD model has proven to be the most accurate among all of the models proposed and investigated in this work. All three models display a similar degree of accuracy after a downstream distance greater than 8D. At the downstream distance greater than 5D, the ability of the radial variation model and modified hybrid model to capture the wake effects shows little difference. However, for a downstream distance of less than 5D, the modified hybrid BEM–AD model provides the most accurate results. Figure 20 shows the centreline downstream velocity and turbulence intensity of the three models against experimental measurements. In Table 5, a statistical analysis is presented for the three studied models which are compared with experimental measurements of centreline downstream velocity and turbulence intensity.

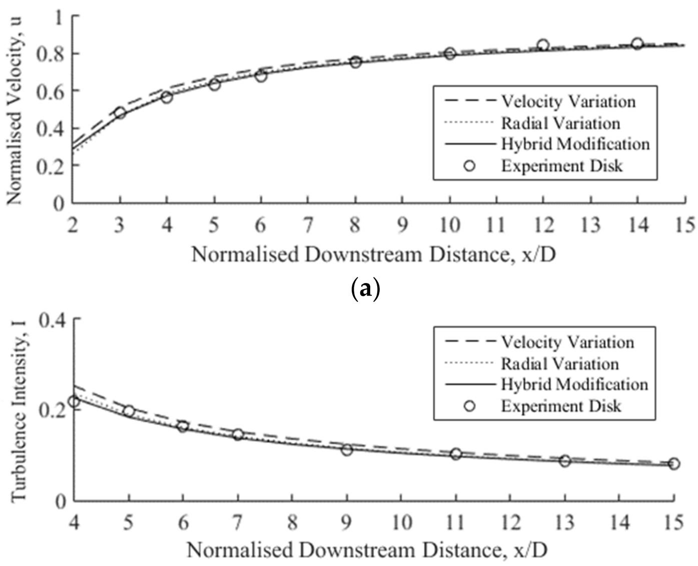

(**a**)

(**b**)

Figure 20. Comparison of downstream centreline (**a**) Velocity and (**b**) Turbulence intensity (bottom) for the velocity variation, radial variation, and hybrid modification against experimental measurements.

Table 5. Statistical analysis of the model for the three models against experimental measurements in terms of downstream centreline velocity and turbulence intensity.

Model	Velocity			Turbulence Intensity		
	R^2	RMSE	MAPE	R^2	RMSE	MAPE
Velocity variation	0.9868	0.0283	3.83%	0.9775	0.0101	6.56%
Radial variation	0.9860	0.0154	1.88%	0.9823	0.0052	3.25%
Hybrid modification	0.9917	0.0131	1.31%	0.0058	0.0045	2.82%

The statistical analysis presented shows that the velocity variation model has the worst correlation and the largest error among all three models, while the radial variation model and the hybrid modified model show very similar correlation and error when compared with the experimental measurements. The hybrid modified model correlates best with the experimental measurements in terms of both downstream velocity and turbulence intensity with a coefficient of determination, R^2 value of 0.9917 and 0.9863, respectively. The hybrid modified model has the smallest error among all three models, with root-mean-square error values of 0.0131 and 0.0058 and mean absolute percentage error (MAPE) values of 1.31% and 2.82% for velocity and turbulence intensity, respectively.

Figures 21 and 22 show contours of velocity and turbulence intensity comparison between radial variation and hybrid modified models. Radial variation models have a more intense turbulence intensity than the hybrid modified model; this will decrease the rate of wake velocity recovery, and it is reflected in the velocity contour. Furthermore, the hybrid modified model shows a shorter contour shape than the radial variation model.

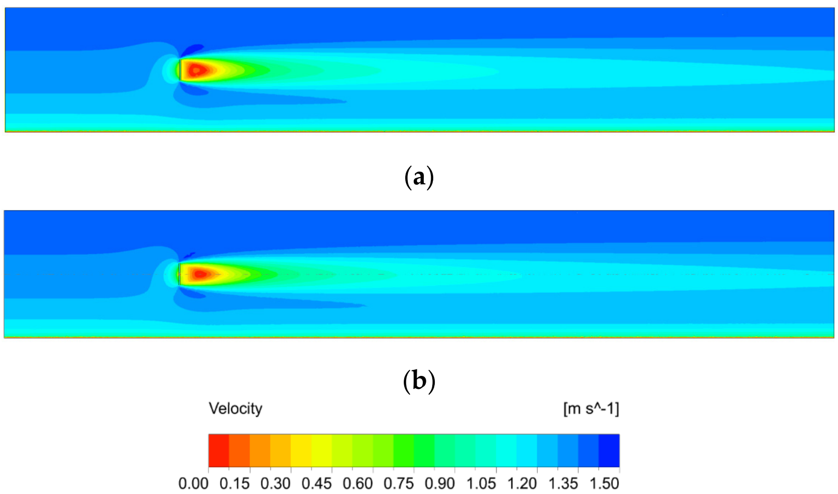

Figure 21. Velocity contour of (**a**) Radial variation model and (**b**) Hybrid modified model from the side view.

Figure 23 shows the power density of the disk for the three studied models. It is observed that the velocity variation disk has a high-power density near the edge of the disk when compared to the other two models. This is due to the velocity variation disk not taking radial blade element characteristics into account. Thus, some BEM-calculated parameters were neglected, such as tip loss correction, while the radial variation model and the hybrid modified model were able to address the tip loss issues. Table 6 is a comparative analysis of the overall thrust and power coefficient of the disk in the three studied models compared with a BEM numerical model discussed in this work. Table 6 shows that all three models have a lower thrust coefficient prediction than the numerical value, which were 0.7571, 0.6278, and 0.7919, respectively; and the velocity variation and hybrid modification models have a higher power coefficient prediction than the numerical value, which were 0.5229 and 0.4714, respectively; while the radial variation model has a lower power coefficient prediction than the numerical value, which was 0.4616.

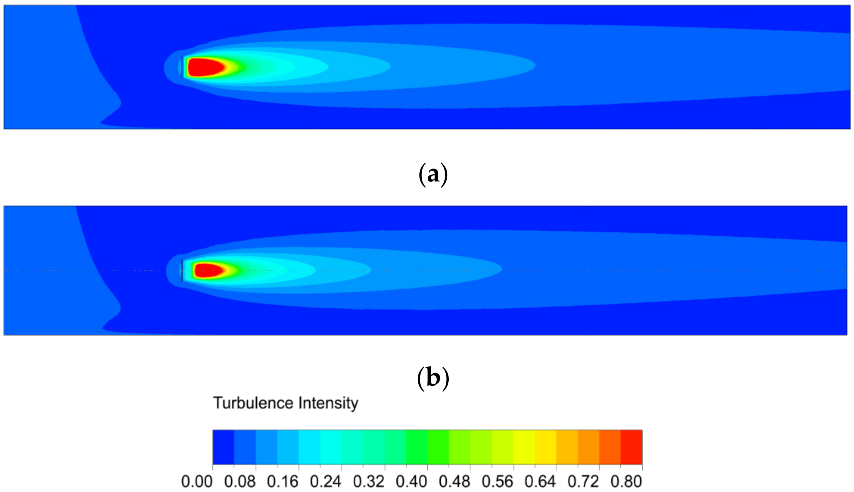

Figure 22. Turbulence intensity contour of (**a**) Radial variation model and (**b**) Hybrid modified model from the side view.

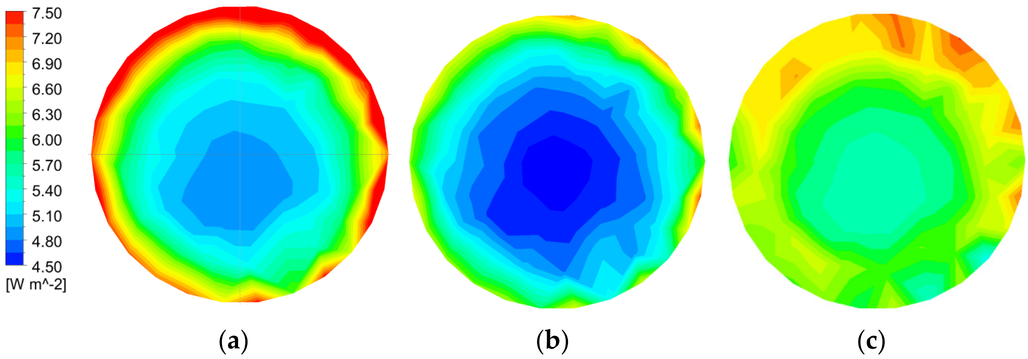

Figure 23. Disk Power density contour of (**a**) Velocity variation model, (**b**) Radial variation model, and (**c**) Hybrid modified model.

Table 6. Comparative analysis of the model for the three studied models against a numerical BEM model in terms of overall thrust and power coefficient of the disk.

Model	Overall Thrust Coefficient		Overall Power Coefficient	
	C_T	ΔC_T	C_P	ΔC_P
BEM	0.7960	-	0.4680	-
Velocity Variation	0.7571	4.89%	0.5229	11.73%
Radial Variation	0.6278	21.13%	0.4616	1.37%
Hybrid Modification	0.7919	0.51%	0.4714	0.72%

The radial variation has the highest difference with the numerical value in terms of thrust coefficient, which was 21.13%, and the velocity variation has the highest difference with the numerical value in terms of power coefficient, which was 11.73%. These indicate that the velocity variation model which incorporates the inflow velocity profile in describing the disk has predicted the thrust more accurately than the radial variation model. The radial variation model, which incorporates radial blade element characteristics in describing the disk, has predicted power better than the velocity variation model. Overall, the hybrid modification model has the least difference when compared with the numerical thrust and power coefficient, which were 0.51% and 0.72%, respectively. Hence, the hybrid modification model has the advantage of both velocity and radial variation due to the incorporation of radial blade element characteristics and inflow velocity profile in describing the disk. However, the hybrid modification model requires more setup and takes longer to solve than velocity and radial variation. Hence, the velocity variation can be used in cases which require good thrust coefficient calculations, while the radial variation can be used in cases which require good power coefficient calculations.

Figure 24 presents the side-view power density contour of the hybrid modified model. The contour in Figure 24 gives a good illustration of the available power density downstream from the disk, as observed as the wake develops further downstream from the disk, the available power from the wake also recovered. Table 7 shows the power coefficient performance of a second disk at downstream distances of 5D, 8D, 10D, and 15D at different heights. It is observed that at a disk vertical offset distance of +1.0 D, the second disk was mostly unaffected by the downstream wake of the first disk and has a difference of less than 2.0% compared to the performance of the first disk. Whereas, it is seen from Table 7 that a positive vertical offset of the second disk has a better performance than a negative vertical offset. At the vertical offset distance of –1.0D, the second disk was least affected by the downstream wake of the first disk but was influenced by the bottom surface and has a difference of less than 27.1% compared to the performance of the first disk.

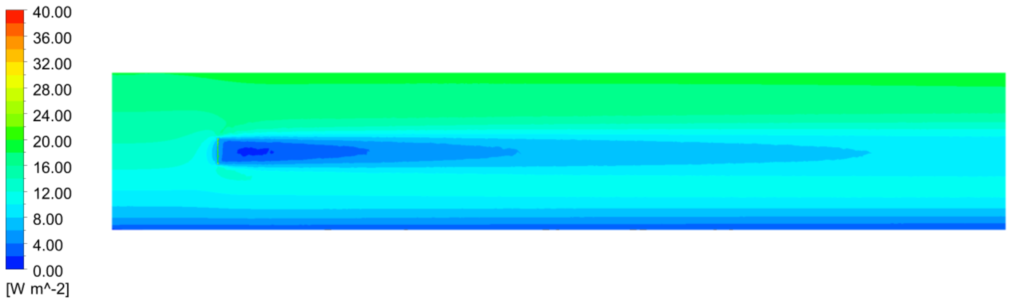

Figure 24. Power density contour of the hybrid modified model from the side view.

Table 7. Comparative analysis of the power coefficient of the second disk at various downstream distances compared to the performance of the first disk.

Disk Vertical Offset	Overall Disk Power Coefficient at Downstream Distance							
	5D		8D		10D		15D	
	C_P	ΔC_P	C_P	ΔC_P	C_P	ΔC_P	C_P	ΔC_P
+1.0 D	0.472	0.1%	0.467	0.9%	0.466	1.2%	0.463	1.9%
+0.5 D	0.288	38.9%	0.304	35.6%	0.312	33.8%	0.328	30.5%
0.0 D	0.172	63.3%	0.207	56.2%	0.225	52.4%	0.256	45.7%
−0.5 D	0.240	49.2%	0.258	45.2%	0.267	43.4%	0.283	40.0%
−1.0 D	0.348	26.2%	0.347	26.5%	0.346	26.7%	0.344	27.1%

7. Conclusions

The work presented in this paper demonstrates the ability of the modified actuator disk models to predict the wake effects of a tidal stream turbine. The hybrid modified model is the most accurate approach to predict the time-averaged velocities and turbulence intensities in the wake of a turbine; however, the pre-solver configuration of the hybrid modified model is more complex compared to the velocity and radial variation model. The results between the three models show very little difference in wake velocity at the downstream distance greater than 5D. For investigations of the far-wake region (greater than 5D), the velocity and radial variation model is a more computational efficient approach. For situations where the velocity profile is constant throughout the whole depth, a radial variation approach can be adopted, while for situations where the velocity profile is varying, a velocity variation approach can be adopted. On the other hand, the hybrid modified model is suitable for investigations for the near-wake region (less than 5D).

These studies also reveal a strong relationship between turbulence intensity and wake velocity recovery rate. A less-intense turbulence after the disk will promote the wake velocity to recover rapidly, and the intensity of the turbulence after the disk is hugely influenced by the porosity and loss coefficient of the disk domain. As a result of these findings, a much more in-depth investigation is needed to investigate the relationship of porosity and loss coefficient of the disk domain with the downstream turbulence intensity. At an offset vertical distance greater than 1D, placement of a second turbine anywhere downstream would yield little difference, while for an offset vertical distance between 0.5D and 1D, a downstream distance greater than 8D would be a better placement for a second turbine. This requires further investigation such as the effects of sitting multiple turbines in the flow field, the effect of yaw misalignment, and also predicting the array layout and power output of a real tidal current energy site. Other areas of interest for further work include an investigation to improve the BEM numerical model to address some of the underprediction issues on thrust coefficient when the tip speed ratio is greater than 8. Also, an investigation into the impact of different turbulence models in predicting the downstream wake development would be valuable.

Author Contributions: Conceptualization, C.M.P., D.M.K. and F.O.; Methodology, C.M.P., D.M.K. and F.O.; Software, C.M.P.; Validation, C.M.P.; Formal analysis, C.M.P.; Investigation, C.M.P., D.M.K. and F.O.; Resources, F.O.; Data curation, C.M.P. and F.O.; Writing—original draft, C.M.P.; Writing—review & editing, C.M.P., D.M.K. and F.O.; Supervision, D.M.K. and F.O.; Project administration, F.O.; Funding acquisition, F.O. All authors have read and agreed to the published version of the manuscript.

Funding: This research was funded internally through the research and graduate studies office at Dundalk Institute of Technology.

Data Availability Statement: Data are contained within the article.

Conflicts of Interest: The authors declare no conflict of interest.

References

1. O'Rourke, F.; Boyle, F.; Reynolds, A. Tidal current energy resource assessment in Ireland: Current status and future update. *Renew. Sustain. Energy Rev.* **2010**, *14*, 3206–3212. [CrossRef]
2. Gaurier, B.; Carlier, C.; Germain, G.; Pinon, G.; Rivoalen, E. Three tidal turbines in interaction: An experimental study of turbulence intensity effects on wakes and turbine performance. *Renew. Energy* **2020**, *148*, 1150–1164. [CrossRef]
3. Zhou, Z.; Benbouzid, M.; Charpentier, J.-F.; Scuiller, F.; Tang, T. Developments in large marine current turbine technologies—A review. *Renew. Sustain. Energy Rev.* **2017**, *71*, 852–858. [CrossRef]
4. Allsop, S.; Peyrard, C.; Thies, P.R.; Boulougouris, E.; Harrison, G.P. Hydrodynamic analysis of a ducted, open centre tidal stream turbine using blade element momentum theory. *Ocean Eng.* **2017**, *141*, 531–542. [CrossRef]
5. The Crown Estate. UK Wave and Tidal Key Resource Areas Project. Available online: https://www.thecrownestate.co.uk/ (accessed on 5 February 2024).
6. Jump, E.; Wills, T.; Macleod, A. Review of tidal turbine wake modelling methods—State of the art. *Int. Mar. Energy J.* **2020**, *3*, 91–100. [CrossRef]
7. Fallon, D.; Hartnett, M.; Olbert, A.; Nash, S. The effects of array configuration on the hydro-environmental impacts of tidal turbines. *Renew. Energy* **2014**, *64*, 10–25. [CrossRef]
8. Bahaj, A.S.; Molland, A.F.; Chaplin, J.R.; Batten, W.M.J. Power and thrust measurements of marine current turbines under various hydrodynamic flow conditions in a cavitation tunnel and a towing tank. *Renew. Energy* **2007**, *32*, 407–426. [CrossRef]
9. Stallard, T.; Collings, R.; Feng, T.; Whelan, J. Interactions between tidal turbine wakes: Experimental study of a group of three-bladed rotors. *Philos. Trans. R. Soc. A Math. Phys. Eng. Sci.* **2013**, *371*, 20120159. [CrossRef] [PubMed]
10. Mycek, P.; Gaurier, B.; Germain, G.; Pinon, G.; Rivoalen, E. Experimental study of the turbulence intensity effects on marine current turbines behaviour. Part I: One single turbine. *Renew. Energy* **2014**, *66*, 729–746. [CrossRef]
11. Mycek, P.; Gaurier, B.; Germain, G.; Pinon, G.; Rivoalen, E. Experimental study of the turbulence intensity effects on marine current turbines behaviour. Part II: Two interacting turbines. *Renew. Energy* **2014**, *68*, 876–892. [CrossRef]

12. Giguere, P.; Selig, M.S. *Design of a Tapered and Twisted Blade for the NREL Combined Experiment Rotor*; National Renewable Energy Lab. (NREL): Golden, CO, USA, 1999. [CrossRef]
13. Edmunds, M.; Malki, R.; Williams, A.J.; Masters, I.; Croft, T.N. Aspects of tidal stream turbine modelling in the natural environment using a coupled BEM–CFD model. *Int. J. Mar. Energy* **2014**, *7*, 20–42. [CrossRef]
14. Batten, W.M.J.; Bahaj, A.S.; Molland, A.F.; Chaplin, J.R. Experimentally validated numerical method for the hydrodynamic design of horizontal axis tidal turbines. *Ocean Eng.* **2007**, *34*, 1013–1020. [CrossRef]
15. Tian, W.; VanZwieten, J.H.; Pyakurel, P.; Li, Y. Influences of yaw angle and turbulence intensity on the performance of a 20 kW in-stream hydrokinetic turbine. *Energy* **2016**, *111*, 104–116. [CrossRef]
16. Malki, R.; Williams, A.J.; Croft, T.N.; Togneri, M.; Masters, I. A coupled blade element momentum—Computational fluid dynamics model for evaluating tidal stream turbine performance. *Appl. Math. Model.* **2013**, *37*, 3006–3020. [CrossRef]
17. Turnock, S.R.; Phillips, A.B.; Banks, J.; Nicholls-Lee, R. Modelling tidal current turbine wakes using a coupled RANS-BEMT approach as a tool for analysing power capture of arrays of turbines. *Ocean Eng.* **2011**, *38*, 1300–1307. [CrossRef]
18. Olczak, A.; Stallard, T.; Feng, T.; Stansby, P.K. Comparison of a RANS blade element model for tidal turbine arrays with laboratory scale measurements of wake velocity and rotor thrust. *J. Fluids Struct.* **2016**, *64*, 87–106. [CrossRef]
19. Belloni, C.S.K.; Willden, R.H.J.; Houlsby, G.T. An investigation of ducted and open-centre tidal turbines employing CFD-embedded BEM. *Renew. Energy* **2017**, *108*, 622–634. [CrossRef]
20. Badoe, C.E.; Edmunds, M.; Williams, A.J.; Nambiar, A.; Sellar, B.; Kiprakis, A.; Masters, I. Robust validation of a generalised actuator disk CFD model for tidal turbine analysis using the FloWave ocean energy research facility. *Renew. Energy* **2022**, *190*, 232–250. [CrossRef]
21. Batten, W.M.J.; Harrison, M.E.; Bahaj, A.S. Accuracy of the actuator disc-RANS approach for predicting the performance and wake of tidal turbines. *Philos. Trans. R. Soc. A Math. Phys. Eng. Sci.* **2013**, *371*, 20120293. [CrossRef]
22. Myers, L.E.; Bahaj, A.S. Experimental analysis of the flow field around horizontal axis tidal turbines by use of scale mesh disk rotor simulators. *Ocean Eng.* **2010**, *37*, 218–227. [CrossRef]
23. Troldborg, N.; Sørensen, J.N.; Mikkelsen, R. Actuator line simulation of wake of wind turbine operating in turbulent inflow. *J. Phys. Conf. Ser.* **2007**, *75*, 012063. [CrossRef]
24. Mikkelsen, R. Actuator Disc Methods Applied to Wind Turbines. Ph.D. Thesis, Technical University of Denmark, Kongens Lyngby, Denmark, 2003. [CrossRef]
25. Kang, S.; Yang, X.; Sotiropoulos, F. On the onset of wake meandering for an axial flow turbine in a turbulent open channel flow. *J. Fluid Mech.* **2014**, *744*, 376–403. [CrossRef]
26. Liu, J.; Lin, H.; Purimitla, S.R. Wake field studies of tidal current turbines with different numerical methods. *Ocean Eng.* **2016**, *117*, 383–397. [CrossRef]
27. Li, Y.; Çalışal, S.M. A Discrete Vortex Method for Simulating a Stand-Alone Tidal-Current Turbine: Modeling and Validation. *J. Offshore Mech. Arct. Eng.* **2010**, *132*, 031102. [CrossRef]
28. Li, L.; Li, Q.; Ni, Y.; Wang, C.; Tan, Y.; Tan, D. Critical penetrating vibration evolution behaviors of the gas-liquid coupled vortex flow. *Energy* **2024**, *292*, 130236. [CrossRef]
29. Fan, M.; Sun, Z.; Yu, R.; Dong, X.; Li, Z.; Bai, Y. Effect of leading-edge tubercles on the hydrodynamic characteristics and wake development of tidal turbines. *J. Fluids Struct.* **2023**, *119*, 103873. [CrossRef]
30. Han, W.; Kim, H.; Son, E.; Lee, S. Assessment of yaw-control effects on wind turbine-wake interaction: A coupled unsteady vortex lattice method and curled wake model analysis. *J. Wind. Eng. Ind. Aerodyn.* **2023**, *242*, 105559. [CrossRef]
31. Harrison, M.E.; Batten, W.M.J.; Myers, L.E.; Bahaj, A.S. A comparison between CFD simulations and experiments for predicting the far wake of horizontal axis tidal turbines. *Renew. Power Gener.* **2010**, *4*, 613–627. [CrossRef]
32. Nguyen, V.T.; Guillou, S.S.; Thiébot, J.; Santa Cruz, A. Modelling turbulence with an Actuator Disk representing a tidal turbine. *Renew. Energy* **2016**, *97*, 625–635. [CrossRef]
33. Chawdhary, S.; Hill, C.; Yang, X.; Guala, M.; Corren, D.; Colby, J.; Sotiropoulos, F. Wake characteristics of a TriFrame of axial-flow hydrokinetic turbines. *Renew. Energy* **2017**, *109*, 332–345. [CrossRef]
34. Kang, S.K.; Kim, Y.; Lee, J.; Khosronejad, A.; Yang, X. Wake interactions of two horizontal axis tidal turbines in tandem. *Ocean Eng.* **2022**, *254*, 111331. [CrossRef]
35. ANSYS. *Ansys Release 5.6 Manual: Theory Reference*, 11th ed.; ANSYS Inc.: Canonsburg, PA, USA, 1999.
36. Sun, X.; Chick, J.P.; Bryden, I.G. Laboratory-scale simulation of energy extraction from tidal currents. *Renew. Energy* **2008**, *33*, 1267–1274. [CrossRef]
37. Myers, L.; Bahaj, A.S. Near wake properties of horizontal axis marine current turbines. In Proceedings of the 8th European Wave and Tidal Energy Conference, Uppsala, Sweden, 7–11 September 2009; pp. 558–565. [CrossRef]
38. Taylor, G.I. *The Scientific Papers of Sir Geoffrey Ingram Taylor*; Cambridge University Press: Cambridge, UK, 1963. [CrossRef]
39. Hansen, M. *Aerodynamics of Wind Turbines*; Routledge: London, UK, 2015. [CrossRef]
40. Moriarty, P.J.; Hansen, A.C. *Aerodynamics Theory Manual*; NREL/TP-500-36881; National Renewable Energy Laboratory: Golden, CO, USA, 2005. Available online: http://www.osti.gov/bridge (accessed on 2 August 2023).

41. Apsley, D.D.; Stallard, T.; Stansby, P.K. Actuator-line CFD modelling of tidal-stream turbines in arrays. *J. Ocean Eng. Mar. Energy* **2018**, *4*, 259–271. [CrossRef]
42. Johnson, B.; Francis, J.; Howe, J.; Whitty, J. Computational Actuator Disc Models for Wind and Tidal Applications. *J. Renew. Energy* **2014**, *2014*, 172461. [CrossRef]